# Visualization of Rayleigh–Taylor flows from Boussinesq approximation to fully compressible Navier–Stokes model

You may also be interested in:

Anelastic Rayleigh–Taylor mixing layers
N Schneider and S Gauthier

Transient effects in unstable ablation fronts and mixing layers in HEDP
J-M Clarisse, S Gauthier, L Dastugue et al.

Compressibility effects in Rayleigh–Taylor flows: influence of the stratification
S Gauthier

Compressibility effects in some buoyant flows
S Gauthier, M-A Lafay, V Lombard et al.

Compressibility effects on the Rayleigh-Taylor instability
M.-A. Lafay, B. Le Creurer and S. Gauthier

Direct Numerical Simulations of Rayleigh-Taylor instability
D Livescu, T Wei and M R Petersen

New phenomena in variable-density Rayleigh–Taylor turbulence
D Livescu, J R Ristorcelli, M R Petersen et al.

TURBULENT CONVECTION IN STELLAR INTERIORS. III. MEAN-FIELD ANALYSIS AND STRATIFICATION EFFECTS
Maxime Viallet, Casey Meakin, David Arnett et al.

ON THE INTERACTION BETWEEN TURBULENCE AND A PLANAR RAREFACTION
Bryan M. Johnson

# Visualization of Rayleigh–Taylor flows from Boussinesq approximation to fully compressible Navier–Stokes model

## N Schneider and S Gauthier[1]

CEA, DAM, DIF, F-91297 Arpajon, France

E-mail: Nicolas.Schneider@cea.fr, Serge.Gauthier@cea.fr and Serge.Gauthier@orange.fr

## Abstract

Visualizations of Rayleigh–Taylor turbulent mixing layers are presented. Three Navier–Stokes models are used: Boussinesq, anelastic and fully compressible. Isosurfaces and slices of concentration, vorticity, $Q$-criterion, turbulent kinetic energy, local Taylor-microscale Reynolds number, dissipation, pressure and temperature are displayed. This gives an overall picture of the Rayleigh–Taylor flows where common features and differences between results obtained from these three models are emphasized. In particular, transition to turbulence and compressibility effects, including asymmetry, are shown.

Keywords: visualization, Rayleigh–Taylor, turbulent mixing layers, Q-criterion, compressible flows

(Some figures may appear in colour only in the online journal)

## 1. Introduction

Flow visualization is the set of methods and techniques making flow patterns visible. This is one of the tools classically used to investigate complex fluid flows. This began in the laboratory two centuries ago, and continues today, in particular with computational fluid dynamics, where large-scale data sets are currently obtained on parallel computers (http://en.wikipedia.org/wiki/scientific_visualization). Flow visualization allows us to consider fluid flows in their entirety, and is the only way to have an overall view on a several-terabyte data set.

---

[1] Author to whom any correspondence should be addressed.

Over the last decades, flow visualization for computer-generated data sets has become a branch of computer science. Mathematical algorithms and various techniques have been developed-and are being developed-for revealing flow characteristics. For a short review, see for example, (Etiene *et al* 2013) and references therein. Flow visualization is used by both fluid dynamic researchers and engineers as a tool, but at the same time their results come close to being 'image art', and sometimes fine arts meet fluid dynamics (Hertzberg Sweetman 2005). In the particular case of Rayleigh–Taylor turbulent mixing layers, concentration isosurfaces are widespread in the literature and on the web (see, for example, (http://en. wikipedia.org/wiki/scientific_visualization)), but visualization does not go much beyond such a scalar representation. However, understanding laminar and turbulent fluid flows requires investigating various issues, such as vorticity and detection of vortices, velocity vector fields, turbulent kinetic energy and dissipation.

A classical pitfall to avoid in visualization is the use of the nevertheless very popular 'rainbow' colour map, which is known to obscure and obfuscate the data to be displayed (Borland and Taylor 2007, Moreland 2009). In contrast, it has been shown that a diverging colour map generally performs well in visualizing scientific data (Moreland 2009). Diverging colour maps have two major colour components; the center point of the map is important and the data go above and below this point.

On the other hand, detection of vortices and coherent structures in turbulent flows is a major concern since vorticity does not always correspond to vortices (Jeong and Hussain 1995, Dubief and Delcayre 2000). Several criteria have been tested (minimum pressure, the second eigenvalue of the vorticity tensor and the $Q$-criterion). The $Q$-criterion now seems to be the consensus choice. The quantity $Q$ refers to the second invariant of the velocity gradient tensor $\nabla_i u_j$, $Q = 1/2 \left( \Omega_{ij} \, \Omega_{ij} - S_{ij} \, S_{ij} \right)$, where $\Omega$ and $S$ are respectively the antisymmetric and symmetric parts of $\nabla_i u_j$. Positive values of $Q$ correspond to vortices, while negative values are associated with shear.

The objective of this paper is to visualize laminar and turbulent Rayleigh–Taylor (RT) mixing flows between miscible fluids. In other words, we present a contribution to a 'Gallery of Rayleigh–Taylor Fluid Motion' coming from several large-scale numerical simulations. These data have been obtained from the solution of three models, the Boussinesq and anelastic approximations and the full compressible Navier–Stokes equations (NSE) (Schneider *et al* 2015). By doing so, we give an insight into the structure of turbulence (vortical and dissipative structures, small-scale intermittency, and homogeneity of compressible mixing layers). Others researchers' findings have already been reported (Glimm *et al* 1990, Mellado *et al* 2005, George and Glimm 2005, Jin *et al* 2005, Livescu 2013).

A single-mode RT flow, i.e., the flow obtained with a single Fourier mode seed, is first presented. This flow is obtained using the anelastic model with weak stratification, and these patterns may be viewed as an elementary pattern constitutive of transient mixing layers. In a second step images obtained from a simulation carried out with the Boussinesq approximation, where only the vorticity Kovásznay mode is present (Chu and Kovásznay 1957), are shown and taken as a reference. Visualization of simulations performed with the anelastic approximation, where a rudimentary entropic mode is present in addition to the vorticity mode, is detailed and common features and differences are emphasized. Finally, simulations carried out with the full Navier–Stokes model, where the vorticity, entropic and acoustic modes are present, are also visualized. The open-source application ParaView (http://www. paraview.org/), which contains many standard flow visualization techniques, such as the $Q$-criterion, is used. The default colour map is a diverging one. ParaView also allows high-resolution images, so pictures displayed in this paper can be enlarged several times, as suggested to the reader.
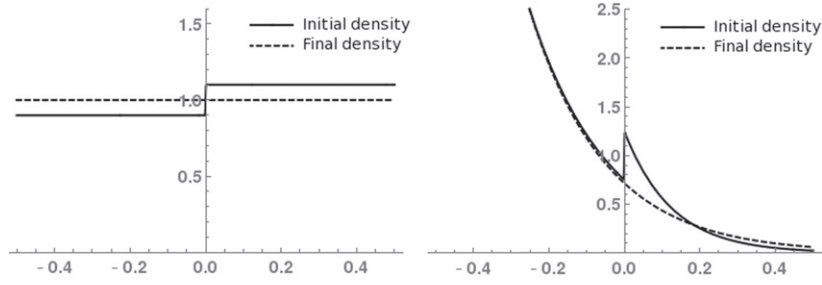
**Figure 1.** Mean density profiles *vs.* the vertical coordinate *z*. Initial density profile of a RT homothermal configuration (full line) and final density profile in dashed line. Left: unstratified profile, the stratification Sr = 0 corresponding to the Boussinesq approximation and the Atwood number At = 0.1. Right: unstable stack of two stable exponentially stratified profiles with Sr = 6 and At = 0.25, corresponding to a highly variable density configuration.

## 2. The Rayleigh–Taylor instability between newtonian fluids

We consider the mixing of two miscible fluids under the action of the Rayleigh–Taylor instability (RTI). The RTI is the potentially unstable superposition of a heavy fluid above a lighter one in a slowly variable acceleration field. Each layer is stably stratified. Such a phenomena on is present in many high-energy-density flows and plays a prominent role, for example, in inertial-confinement fusion and in supernova explosions in astrophysics. It is also a classical fluid dynamic problem (http://www.iwpctm.org/), (Schneider and Gauthier 2015), (http://www.tmbw.org/). RTI flow patterns depend strongly on the initial perturbation between the two fluids. Schematically for large-scale single perturbations, RT flows produce mushroom-like patterns while for small-scale perturbations with a large number of Fourier modes, RT flows may produce homogeneous turbulent mixing layers. At the initial times of the RTI development, the mean density profile undergoes a sharp discontinuity (see figure 1). This density jump decreases with time and at the end of the mixing process, the density is one-dimensional with uniform concentration and temperature. The motion takes place in a three-dimensional closed rectangular domain $L_x \times L_y \times L_z$ ($L_z \equiv h_H - h_L$, where $|h_H|$ and $|h_L|$ are the heights of the heavy and light fluid layers, respectively). The heavy and light fluids are initially located in the upper and lower sides of the computational domain such that $0 \leqslant z \leqslant h_H$ and $h_L \leqslant z \leqslant 0$.

The single-fluid approximation is used and a single velocity field is defined. The mixing is described by the classical thermodynamic model 'partial pressures—partial densities'. It reads $p = p_H + p_L$, $\rho = \rho_H + \rho_L$ and $T = T_H = T_L$, where $p$, $\rho$ and $T$ are the pressure, density and temperature of the single fluid. The symbols $\rho_{H,L}$ and $T_{H,L}$ are the partial densities and the temperatures of the heavy ($H$) and light ($L$) fluids, respectively. The expressions for the partial pressures read $p_{H,L} = \rho_{H,L}(\mathcal{R}/\mathcal{M}_{H,L})T_{H,L}$. A fluid concentration $c = \rho_H/\rho$ is also defined. The specific heats at constant volume and constant pressure are denoted $C_{v,p;H,L}$. Their ratio is $\gamma_{H,L}$. The adiabatic index of the mixing depends on the concentration and is given by $\gamma_m(c) = C_{p,m}/C_{v,m}$, the mixing specific heats being $C_{v,p;m}(c) = c\, C_{v,p;H} + (1 - c)C_{v,p;L}$. The reference concentration is chosen to be $c_{ref} = (1 - \mathrm{At})/2$, where the Atwood number is defined as

$$\text{At} = \frac{\rho_H(z = 0^+, t = 0) - \rho_L(z = 0^-, t = 0)}{\rho_H(z = 0^+, t = 0) + \rho_L(z = 0^-, t = 0)}. \tag{1}$$

We also use the reference values $C_{v,r}(c_{ref})$ and $\gamma_r = \gamma_m(c_{ref})$.

## 2.1. The full Navier–Stokes equations

The full NSEs for a binary mixture may be written in a dimensionless form with the following units. $L_y$ (the horizontal width of the domain) is used for the unit of length, $(L_y/g)^{1/2}$ for time where $g$ is the acceleration due to gravity, the half-sum of densities on each side of the pseudo-interface, $\rho_r = 1/2\,\rho_H(z = 0^+, t = 0) + \rho_L(z = 0^-, t = 0)$, for the mass, and a uniform temperature $T_r = T_H = T_L$. The stratification parameter is $\text{Sr} = g\,L_y/(\mathcal{R}\,T/\mathcal{M}_r)$ with $2/\mathcal{M}_r = 1/\mathcal{M}_H + 1/\mathcal{M}_L$. The full NSEs therefore (Schneider and Gauthier 2015)

$$\partial_t\rho + \partial_j(\rho\,u_j) = 0, \tag{2}$$

$$\rho(\partial_t u_i + u_j\,\partial_j u_i) = -\frac{1}{\text{Sr}}\partial_i p + \frac{1}{\text{Re}}\,\partial_j\sigma_{ij} - \rho\,\delta_{i3}, \tag{3}$$

$$\rho\,(\partial_t e + u_i\,\partial_i e) = -(\gamma_r - 1)p\,\partial_i u_i + (\gamma_r - 1)\frac{\text{Sr}}{\text{Re}}\,\sigma_{ij}\,D_{ij} \tag{4}$$

$$+\frac{\gamma_r - 1}{\text{Sc Re}}\,\partial_i[\Delta_{H,L}^\star\,T\,\partial_i c] + \frac{\gamma_r}{\text{Pr Re}}\,\partial_{ii}^2 T, \tag{5}$$

$$\rho(\partial_t c + u_j\,\partial_j c) = +\frac{1}{\text{Sc Re}}\,\partial_{ii}^2 c, \tag{6}$$

$$p = \rho\,T\,(1 + \text{At} - 2\,\text{At}\,c), \tag{7}$$

where $u_i$ is the $i$th-velocity components. The viscous-stress tensor is $\sigma_{ij} = \mu\,(\partial_j u_i + \partial_i u_j - 2/3\,\partial_\ell u_\ell)$, and $D_{ij} = 1/2(\partial_j u_i + \partial_i u_j)$ is the rate-of-deformation tensor. The difference of specific heats at constant pressure of the two species is $\Delta_{H,L}^\star = (C_{p\,H} - C_{p\,L})/C_{v,r}$. The dimensionless numbers, Re, Pr, Sc and Sr, are given by

$$\text{Re} = \frac{g^{1/2}\,L_y^{3/2}}{\mu/\rho_r}, \quad \text{Pr} = \frac{\mu\,C_p}{\kappa}, \quad \text{Sc} = \frac{\mu}{D}, \quad \text{Sr} = \frac{g\,L_y}{R\,T_r}, \tag{8}$$

where $\mu$, $\kappa$ and $D$ are the coefficients of viscosity, thermal conduction and diffusion of species, respectively. The initial equilibrium state is given by the hydrostatic equilibrium state obtained from equations (2)-(7) by setting the velocity $u_i$ to zero and looking for a stationary solution. This equilibrium state is therefore a potentially unstable stack of two stable exponentially stratified profiles,

$$\overline{\rho}(z) = \overline{\rho}_H(z) + \overline{\rho}_L(z) = (1 + \text{At})\exp(-\text{Sr}_H\,z)H_+(z)$$
$$+ (1 - \text{At})\exp(-\text{Sr}_L\,z)H_-(z), \tag{9}$$

with $\text{Sr}_{H,L} = \text{Sr}/(1 \mp \text{At})$, $H_\pm(z) = (1 \pm H(z))/2$, where $H(z)$ is the Heaviside function. The parameter Sr is called a 'stratification parameter' although the heavy and light fluids undergo a stratification equal to $\text{Sr}_{H,L}$, respectively. The initial temperature profile is uniform: $T_H = T_L = 1$.

The final equilibrium state, i.e., after the overturn of the fluids, is a new stable equilibrium state, which depends only on the vertical $z$-coordinate. In this regime, velocities vanish and density follows an exponential profile denoted $\rho^{(fin)}(z)$. Its expression is

$$\rho^{(fin)}(z) = \rho^{(fin)}(0) \exp(-\mathcal{S} z), \tag{10}$$

where $\mathcal{S} = \mathrm{Sr}\,(1 + \mathrm{At} - 2\,\mathrm{At}c^{(fin)})^{-1}$ with $c^{(fin)} = m_H/(m_H + m_L)$ and $\rho^{(fin)}(0) = (m_H + m_L)\,\mathcal{S}[\exp(-\mathcal{S}\,z_{bot}) - \exp(-\mathcal{S}\,z_{top})]^{-1}$, $m_{H,L}$ being the mass of the heavy and light fluids.

It is well known that the full set of NSEs (2)-(7) contains the three Kovásznay modes (Chu and Kovásznay 1957), i.e., the acoustic, vorticity and entropic modes. In some situations these effects and their coupling are important, but in other situations such complexity is not needed. Moreover the acoustic mode forces a small time step through the CFL condition. Simplified subsets of the full NSEs have been developed in the past for various flows. For the RT flow, we have recently developed three low-Mach-number models for the mixing of two Newtonian fluids (Schneider and Gauthier 2015), i.e., the anelastic, the quasi-isobaric and the Boussinesq models.

The anelastic and Boussinesq models are briefly recalled below.

## 2.2. The anelastic approximation

The anelastic approximation is derived from the full Navier–Stokes equations with an asymptotic analysis performed in terms of the small parameter $\gamma_r\,\mathrm{Ma}^2$, where Ma is a Mach number. The following set of equations has been obtained for the momentum, energy and concentration:

$$\rho^{(0)}(\partial_t u_i^{(0)} + u_j^{(0)}\,\partial_j u_i^{(0)}) = -\mathrm{Sr}^{-1}\,\partial_i p^{(1)} + \mathrm{Re}^{-1}\,\partial_j \sigma_{ij}^{(0)} - \rho^{(1)}\,\delta_{i3}, \tag{11}$$

with the constraint $\partial_i(\rho^{(0)}\,u_i^{(0)}) = 0$;

$$\begin{aligned}
\partial_t \rho^{(0)}\,e^{(1)} + \partial_i \rho^{(0)}\,u_i^{(0)}\,e^{(1)} &= -(\gamma_r - 1)p^{(1)}\,\partial_i u_i^{(0)} \\
&+ \frac{\gamma_r}{\mathrm{Pr}\,\mathrm{Re}}\,\partial_{ii}^2 T^{(1)} + (\gamma_r - 1)\frac{\mathrm{Sr}}{\mathrm{Re}}\,\sigma_{ij}^{(0)}\,D_{ij}^{(0)} \\
&+ \frac{\Delta_{H,L}^\star}{\mathrm{Sc}\,\mathrm{Re}}\,\partial_i[T^{(0)}\,\rho^{(0)}\,\partial_i c^{(1)}],
\end{aligned} \tag{12}$$

where $e^{(1)}$ is the internal energy at first order;

$$\rho^{(0)}(\partial_t c + u_j^{(0)}\,\partial_j c) = \frac{1}{\mathrm{Sc}\,\mathrm{Re}}\,\partial_i(\rho^{(0)}\,\partial_i c). \tag{13}$$

'The EOS

$$\frac{p^{(1)}}{p^{(0)}} = \frac{\rho^{(1)}}{\rho^{(0)}} + \frac{T^{(1)}}{T^{(0)}} - \frac{2\,\mathrm{At}\,c^{(1)}}{1 + \mathrm{At} - 2\,\mathrm{At}\,c^{(0)}}, \tag{14}$$

which is defined for Atwood numbers strictly smaller than one, i.e., $\mathrm{At} < 1$. The full thermodynamic quantities read

$$\begin{aligned}
\rho &= \rho^{(0)} + \rho^{(1)}, & c &= c^{(0)} + c^{(1)}, \\
p &= p^{(0)} + p^{(1)}, & T &= T^{(0)} + T^{(1)}.
\end{aligned} \tag{15}$$

## 2.3. The boussinesq approximation

The simplest model for RT configurations, called the Boussinesq approximation, is obtained in the limit of vanishing stratification and Atwood numbers and infinite ratio of specific heats, $\gamma_r$. Physical quantities are expanded in powers of the Atwood number, $p = p^{(0)} + p^{(1)}\,\mathrm{At} + p^{(2)}\,\mathrm{At}^2 + \ldots$ (Schneider and Gauthier 2015). One thus gets two

**Table 1.** Simulation definition. The first column refers to simulation names. The first letter stands for the physical model, $B$ for the Boussinesq model, $A$ for the anelastic and $C$ for the full compressible case. The Reynolds and Atwood numbers, the stratification, the amplitude and the wave numbers defining the initial condition, and the largest spatial resolution used are given from left to right. The last column refers to the highest Taylor $z$-microscale Reynolds number reached, $Re_{\lambda_z} = Re\,\lambda_{zz}\,\sqrt{2\,\tilde{k}}$, with $\lambda_{zz}^2 = \langle \overline{u_z''^{\,2}} \rangle / \langle \overline{(\partial u_z''/\partial z)^2} \rangle$, where $\langle\rangle$ is the $xyz$ mean value. The Favre fluctuation and mean value are denoted $''$ and $\sim$, respectively.

| Name | Re | At | Sr | $x_{\mathrm{init}}$ | $[k_{\min}, k_{\max}]$ | $N_z \times N_x \times N_y$ | $Re_{\lambda_z}$ |
|---|---|---|---|---|---|---|---|
| AC | $5.10^3$ | 0.20 | 0.2 | $-0.010$ | $[2\,\pi,\,2\,\pi]$ | $(10 \times 64) \times 384^2$ | $\times$ |
| BF | $3.10^4$ | 0.10 | 0.0 | $''$ | $[151, 182]$ | $(24 \times 40) \times 940^2$ | 142 |
| AF | $''$ | 0.25 | 2.0 | $''$ | $''$ | $(20 \times 48) \times 600^2$ | 131 |
| AI | $''$ | 0.50 | $''$ | $''$ | $''$ | $(14 \times 48) \times 600^2$ | 220 |
| CF | $''$ | 0.25 | 6.0 | $-0.040$ | $''$ | $(6 \times 64) \times 384^2$ | 49 |
| CG | $6.10^4$ | $''$ | $''$ | $-0.001$ | $''$ | $(9 \times 100) \times 1000^2$ | 56 |

equations:

$$\partial_t u_i^{(0)} + u_j^{(0)}\,\partial_j u_i^{(0)} = -\,\partial_i p^{(2)} + Re^{-1}\,\partial_{jj}^2 u_i^{(0)} - (2\,c^{(0)} - 1)\,\delta_{i3},$$

and, with the constraint,     $\partial_i u_i^{(0)} = 0,$

$$\partial_t c^{(0)} + u_j^{(0)}\,\partial_j c^{(0)} = (Sc\,Re)^{-1}\,\partial_{ii}^2 c^{(0)}. \tag{16}$$

In the next sections, we report visualization of RT flows obtained with the Boussinesq and anelastic models and with the full NSEs.

## 3. Numerical simulations

The numerical methods developed to solve these three models, within the framework of spectral methods, have been previously detailed in (Gauthier *et al* 2005, Le Creurer and Gauthier 2008, Schneider *et al* 2015). These methods have been implemented in the code AMENOPHIS (Gauthier *et al* 2005, Le Creurer and Gauthier 2008), which uses a variable spatial resolution. Therefore simulations are started with a low resolution and the resolution is increased with the flow development. For example, simulation AF (see table 1) was started with $(8 \times 32) \times 256^2 = 17\,M$ collocation points and after several Chebyshev-Fourier mode number increases it reaches $(20 \times 48) \times 600^2 = 345\,M$ (factor 20). The six simulations reported in this paper are summarized in table 1. The simulation BF carried out within the Boussinesq approximation is the reference used for the remainder of this paper. This is the simplest model with no stratification, thermodynamics, or acoustics. A turbulent state has been reached, attested to by the Reynolds number. Simulations are initialized with a solenoidal velocity vector field. Two different velocity perturbations are used and they are characterized by their Fourier spectrum: single-mode (a single Fourier mode) or multi-mode. The latter is built with a set of Fourier modes, $(k_x, k_y)$, whose amplitudes are chosen randomly within the annulus $k_{\min} \leqslant \sqrt{k_x^2 + k_y^2} \leqslant k_{\max}$. As can be seen in table 1, only large wave numbers are used. The perturbation is restricted to the vicinity of the plane $z = 0$ through the function $\cosh^{-1}(z/\delta)$, where $\delta$ is the thickness of the perturbation.

### 3.1. Validation and verification

Validation against RT flow experimental data is limited since such data are fairly scarce and are restricted to unstratified configurations. Such a validation has nevertheless been achieved for the nonlinear growth rate $\alpha_b$ and is detailed in (Mueschke *et al* 2006, Mueschke and Schilling 2009, Glimm *et al* 2013). The algorithm for the Boussinesq approximation and the numerical code used for the visualizations presented in this paper have been validated against the Waddell *et al* laminar single-mode experiment (Waddell *et al* 2001). The nonlinear growth rate $\alpha_b$ of a turbulent RT mixing layer has also been computed and was found to be close to $\alpha_b = 0.021$, which is in good agreement with experimental data (Schneider *et al* 2015, Schneider 2015, Schneider and Gauthier 2015). More generally, this analysis gives a coherent view of RT turbulence. On one hand, it agrees with other RT numerical simulations for what it is known (mixing length, mixing fraction, etc) and on the other hand it agrees with classical results on turbulent flows (spectra, PDFs, etc).

Some verification steps have also been carried out. Let us first recall that the algorithms for the Boussinesq and the anelastic approximations and the fully compressible option are embedded in the same code. In particular they share the same derivative operators and the same auto-adaptive grid generation algorithm. We have shown within the anelastic option that spectral accuracy is achieved by plotting Chebyshev coefficients versus the spatial frequency. We have also shown that the error in the momentum divergence decays exponentially with the number of Chebyshev modes. Temporal convergence has been studied and was found to approach the second-order accuracy. The Boussinesq option is obtained from the anelastic option by using a uniform mean density $\rho^{(0)}$. The compressible option has been first verified against linear stability results (Le Creurer and Gauthier 2008) for a 2D single-mode simulation. These results were obtained with a stability code analysis, based on the normal mode method. The correct decay rate of the kinetic energy after overturn of the two fluids also provides a verification of the accuracy ((Le Creurer and Gauthier 2008), figure 21).

## 4. Single-mode anelastic simulation: AC

Visualization of RT flows begins with a numerical simulation seeded with a single Fourier mode. Density and concentration take the form of the classical buoyancy pattern-a mushroom-like structure or a plume-as shown in figure 2 (left). Due to the finite value of the Atwood number (At = 0.20) there is a slight compressibility effect, which results in a slight asymmetry with respect to the plane $z = 0$. Therefore, for clarity, the picture is given with gravity directed upward. Consequently the heavy fluid goes from bottom to top of the image while the light fluid moves in the opposite direction. The head of the mushroom of heavy fluid is classically called the 'spike' and the light fluid pattern is called 'bubble'. The pattern is coloured to show the velocity divergence, $\partial_i u_i$, so that compressed regions are shown in red, while expanded regions are shown in blue. The right part of the same figure displays the isosurface of the $x$-component of the vorticity, $\omega_x$. This helps in understanding the vortical structure of a single-mode RTI. The $x$ and $y$ vorticity components are equal and are much larger than the $z$-component. The vorticity norm leads to a toroidal isosurface (not represented here), while the horizontal components lead to this 'double-spoon' pattern, one being positive, the other negative (figure 2, right). The $y$-component gives the same picture, in such a way that the two 'double-spoon' patterns form a torus.

As we have already discussed, vortices are better detected by the $Q$-criterion. Figure 3 displays an isosurface of this $Q$-criterion coloured by concentration. A torus appears very clearly in the center of the domain and four quarters of this ring also appear, one in each
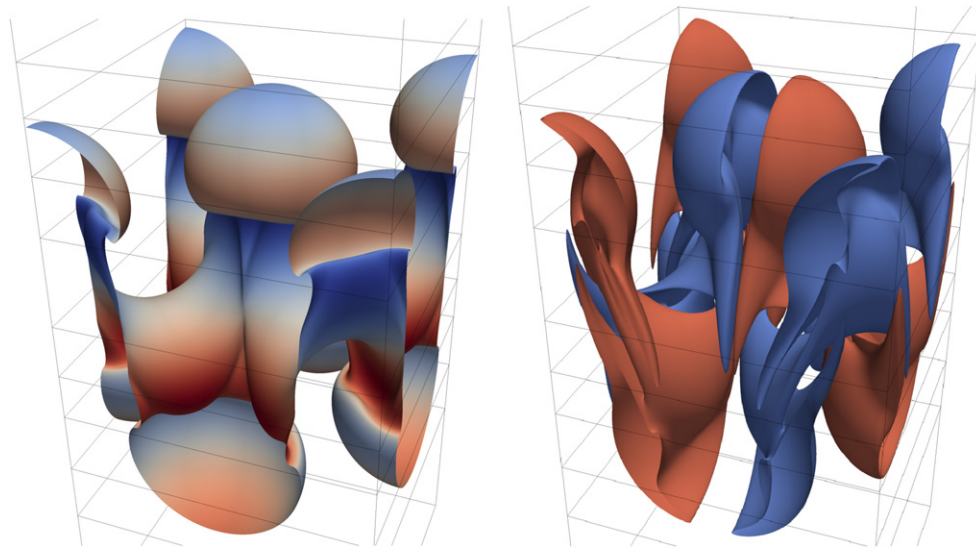
**Figure 2.** Simulation AC. Left: concentration isosurface $c = 0.5$, coloured based on the velocity divergence $\partial_i u_i$. Right: $\omega_x = \pm 3x$-vorticity component isosurfaces, coloured by the sign of this quantity. Gravity is directed upward. Horizontal black lines are the boundaries between the Chebyshev numerical subdomains.

corner (the computation is periodic in the horizontal plane), with the heavy fluid inside and the light fluid outside. In addition, four sets of two vortices are placed in such a way that they form a stool. Stream lines at a given time (the flow is unsteady) have been added to this picture (in one quarter), also coloured to show concentration. One thus clearly sees the heavy fluid moving upward into the light fluid.

## 5. Boussinesq simulation: BF

This section is devoted to the Boussinesq simulation. Concentration, vorticity, $Q$-criterion, velocity, turbulent kinetic energy, local Taylor-microscale Reynolds numbers and dissipation are successively displayed and commented. Some of these features have already been observed by other investigators (Young *et al* 2001, Ristorcelli and Clark 2004, Vladimirova and Chertkov 2009).

### 5.1. Concentration

The two concentration isosurfaces of $c = 0.02$ and $c = 0.98$ are represented in figure 4. A top view is used on the left (gravity directed downward) so that the $c = 0.98$-isosurface appears on the top, while a bottom view is used on the right (gravity directed upwards), so the $c = 0.02$-isosurface appears on the top. These isosurfaces are located close to the boundaries, or are the frontiers themselves, of the turbulent mixing layer, where turbulence is vanishing. As a result, flow is essentially made of large structures. In particular, the centers of mushrooms are minima of the vorticity according to the isovorticity-torus shape. Patterns on the top and bottom of the layer look very similar. This symmetry is expected from the Boussinesq approximation. Consequently only top views are given in this section, after figure 4.
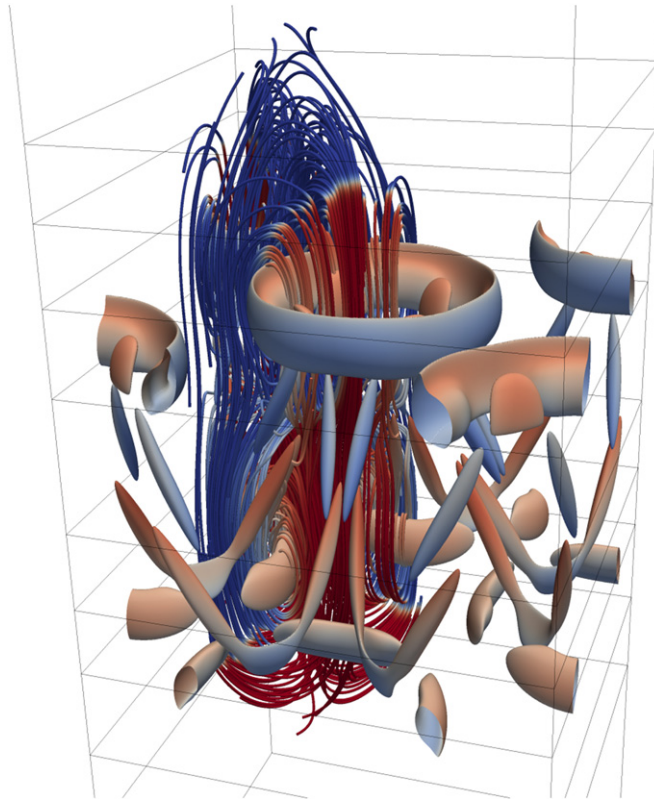
**Figure 3.** Simulation AC: $Q$-criterion isosurface with $Q = 10$, with stream lines in a quarter of the simulation domain. Isosurface and streamlines are coloured by the concentration (heavy fluid in red and light fluid in blue). Gravity is directed upward. Horizontal black lines are the boundaries between the Chebyshev numerical subdomains.

The concentration on the $z = 0$-plane in figure 5 reveals unmixed $(x, y)$-regions although turbulence is well developed and is at a maximum at this height. Heavy (resp. light) fluid appears in red (resp. blue), and the higher the plane the larger the regions of pure heavy fluid. On the $z = 0.35$-plane, close to the mixing layer boundary, one distinguishes the twisted and bent mushrooms visible in figure 4.

### 5.2. Vorticity

Vorticity is a vectorial quantity, so the norm and the three components may be displayed. However, since the flow is homogeneous on a horizontal plane, the $x$- and $y$-components give very similar or identical results. Moreover, within the Boussinesq approximation, heavy and light fluid flows are symmetrical with respect to each other. Vorticity $x$-component iso-surfaces are displayed in figure 6 at an intermediate time, before turbulence is fully developed. This picture clearly shows a multi-'double-spoon' structure, as identified in the single-mode numerical simulation (figure 2), although the spoons are deformed by the growing turbulence. The vorticity norm is displayed on the left side of figure 7 with a low value, $|\omega| = 3$, so that large structures, with the torus shape corresponding to mushroom-like
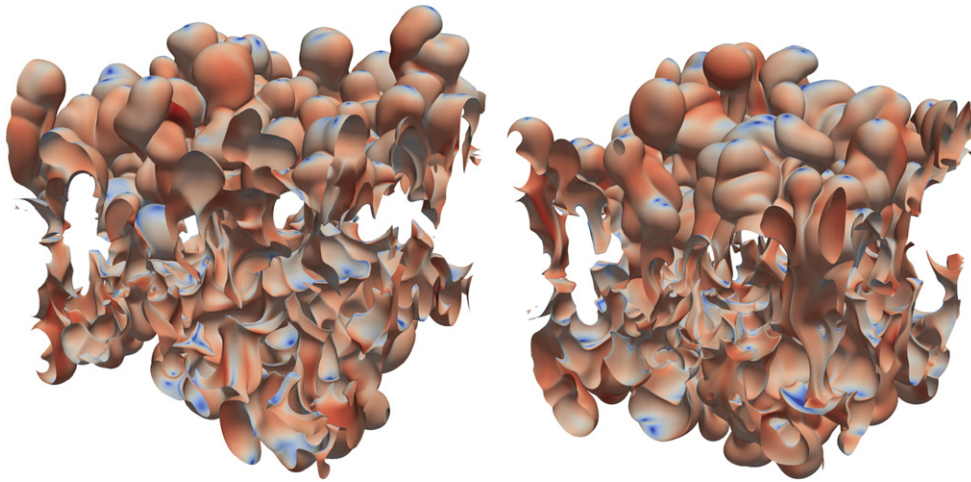
**Figure 4.** Simulation BF: concentration isosurfaces, $c = 0.02$ and $c = 0.98$, coloured by the vorticity (log scale, blue: $\omega = 0.04$, red: $\omega = 4$). Final time of the simulation. Left: top view; right: bottom view.
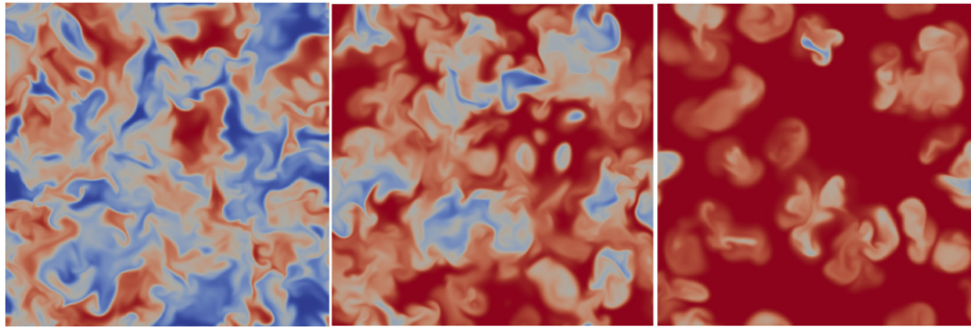


**Figure 5.** Simulation BF: concentration on the $z = 0$-plane (left), $z = 0.2$-plane (middle) and $z = 0.35$-plane (right). Heavy fluid is coloured red ($c = 1$) and light is coloured blue ($c = 0$). Final time of the simulation.

structures, appear clearly on the boundaries. For a larger isovalue of the vorticity norm, $|\omega| = 20$, on the right of figure 7, the RT patterns on the boundaries disappear, and iso-surfaces become lighter and tend to be oblong or take the form of short filaments attached to the mixture dominated either by the heavy (red) or by the light fluid (blue). At this level, turbulence is expected to be more isotropic and more universal. These pictures show that the vortical structure of RT turbulence is qualitatively similar to other turbulent flows. Large-scales the mushroom-like structures bear the track of the instability that generates turbulence. Intermediate scales are associated with random interactions while small scales have some coherence as shown in the right part of figure 7 (She *et al* 1990). Figure 8 compares the $x$- and $z$-vorticity components for the value $\omega_{x,z} = 10$. The $x$-component appears to be stronger than the $z$ one and the double-spoon structure on the $x$-component is no longer visible.

Figure 9 (left) displays a slice of vorticity in a vertical $(y, z)$-plane, where the mushroom shape is visible with some points of intense vorticity. The inhomogeneous character of the
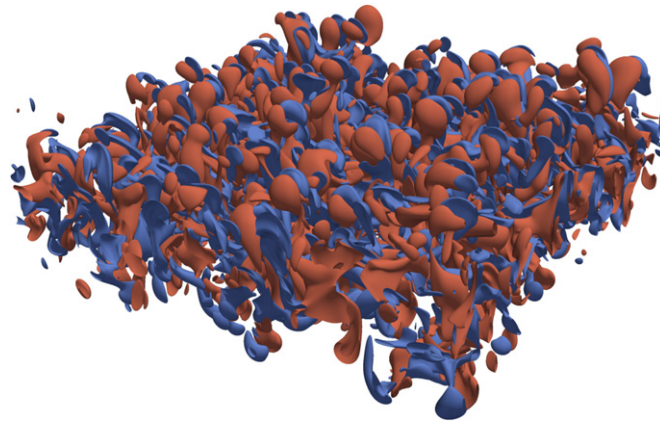
**Figure 6.** Simulation BF: vorticity $x$-component isosurfaces for $\omega_x = -5$ and $\omega_x = 5$. Intermediate time at which the transition to turbulence is occurring. Red stands for positive values and blue for negative ones.
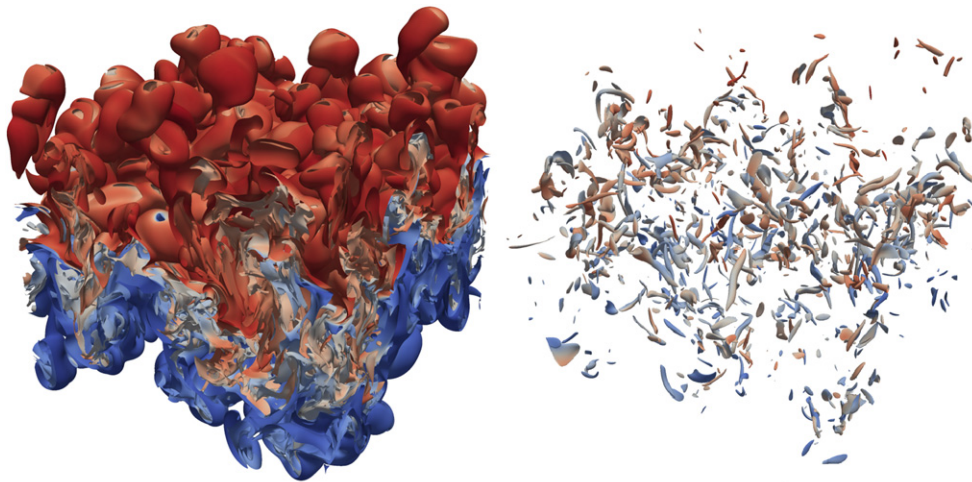


**Figure 7.** Simulation BF: vorticity isosurface, top view. Left: $|\omega| = 3$. Right: $|\omega| = 20$, coloured by the concentration. Final time of the simulation.

mixing layer should also be noted; some vorticity structures have escaped from the mixing layer. In the same figure 9 (middle), in the $z = 0$-plane, turbulence appears to be well developed with a strong inhomogeneous vorticity distribution. Away from the center and close to the boundary, figure 9 (right) exhibits only a few patterns. In figure 10, the velocity vector field is superimposed on the vorticity field and a zoom is presented. A subset has been extracted from the whole simulation domain by defining a small box such that $0 < x, y < 0.319$ and $-0.117 < z < 0.133$. Figure 10 left is the horizontal $(x, y)$-plane at the middle of the small box, while the right picture is the vertical $(y, z)$-mid-plane of the small box. Positive (resp. negative) vorticity values appear in red (resp. blue). The velocity vector field rolling round vortices of positive or negative values of vorticity can be seen clearly.
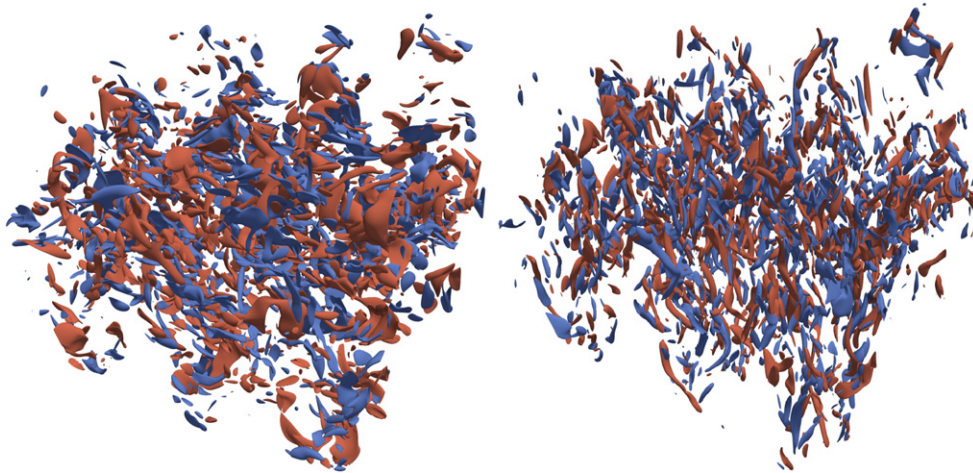
**Figure 8.** Simulation BF. Left: isosurfaces of $x$-component of vorticity $\omega_x = -10$ and $\omega_x = 10$. Right: isosurfaces of $x$-component of vorticity $\omega_z = -10$ and $\omega_z = 10$. Blue stands for negative vorticity values and red for positive ones. Final time of the simulation.
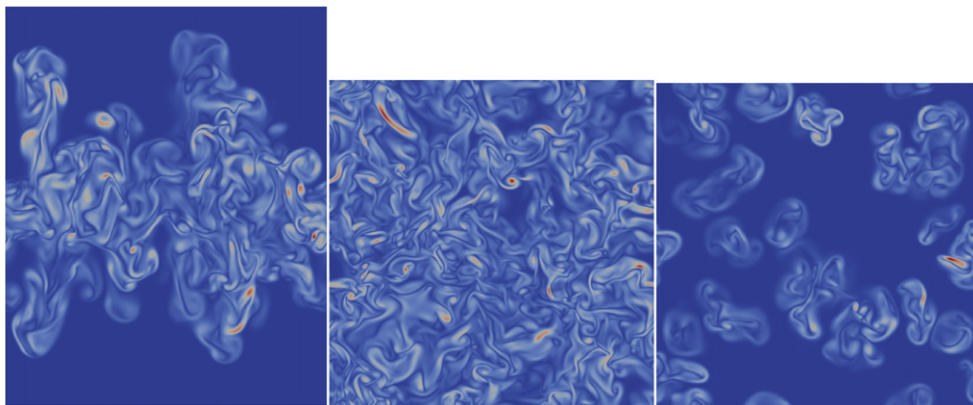


**Figure 9.** Simulation BF: slices of vorticity. Left: vertical $(y, z)$-plane. Middle: horizontal $z = 0$-plane. Right: horizontal $z = 0.35$-plane. Final time of the simulation.

There are also some 3D effects, for example in the bottom right part of the left-hand picture, where the fluid moves normally to the slice and along the gravity direction.

### 5.3. Q-criterion

The $Q$-criterion is displayed in figure 11 for two values $Q = 30$, and $Q = 50$. On the left, the small value of $Q$ allows us to capture a large number of vortices. Some are close to the boundaries and are made of pure fluid, either heavy (red) or light (blue). On the right, the large value of $Q$ selects more intense vortices, which are less dense. Actually, there is some homothety between these two pictures. In both cases, it is worth noticing the oblong shapes of the vortices.
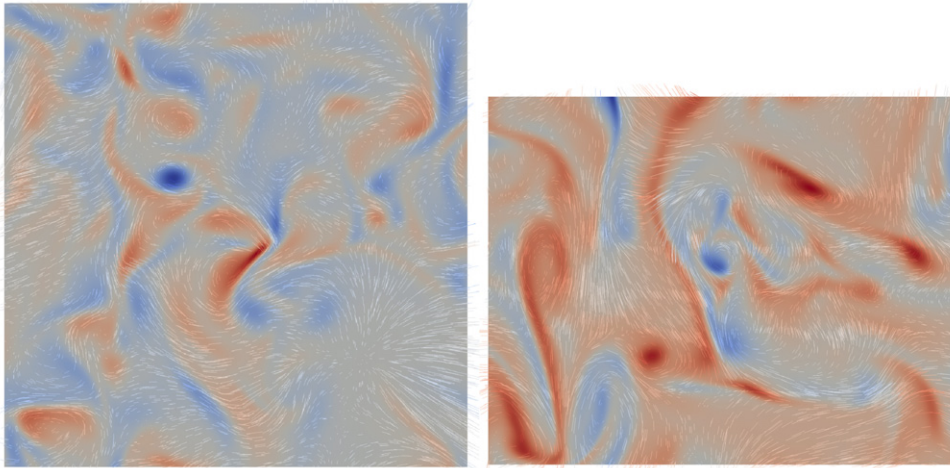
**Figure 10.** Simulation BF: slices of vorticity with the velocity vector field. Left: horizontal $(x, y)$-mid-plane. Right: vertical $(y, z)$-plane. These slices are extracted from a subset of the total simulation box: $0 < x, y < 0.319$ and $-0.117 < z < 0.133$. Final time of the simulation.
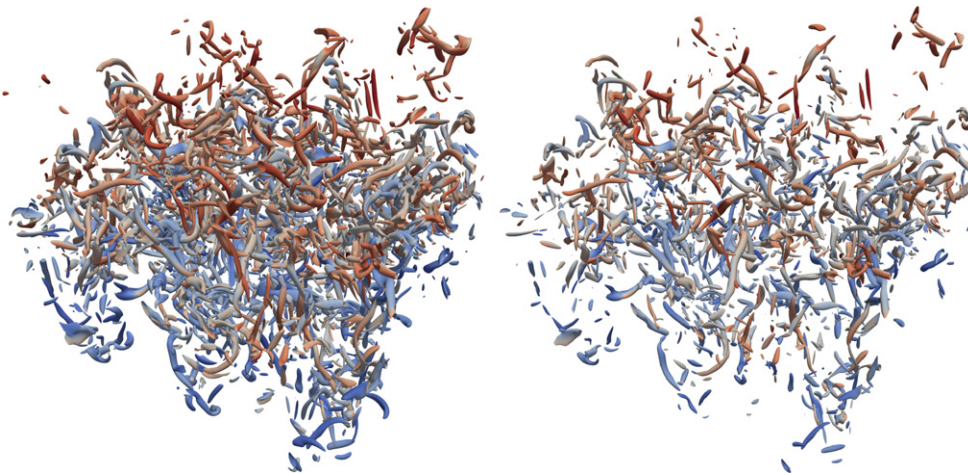


**Figure 11.** Simulation BF: isosurface $Q$-criterion coloured by the concentration (heavy fluid in red and light fluid in blue). Left: $Q = 30$. Right: $Q = 50$. Final time of the simulation.

## 5.4. Velocity

Figure 12 displays, from left to right, the velocity norm, $|u|$ ($u$ is the total velocity), and two components, $u_x$ and $u_z$. On the left, the velocity norm $|u|$ appears to be quite inhomogeneous with some spots of intense velocity in red, while regions at rest are shown in blue. As expected, the vertical velocity (right) is much stronger than the horizontal component (middle), since the same colour scale has been used. We observe ascending and descending fluid motion, and regions at rest appear in white.
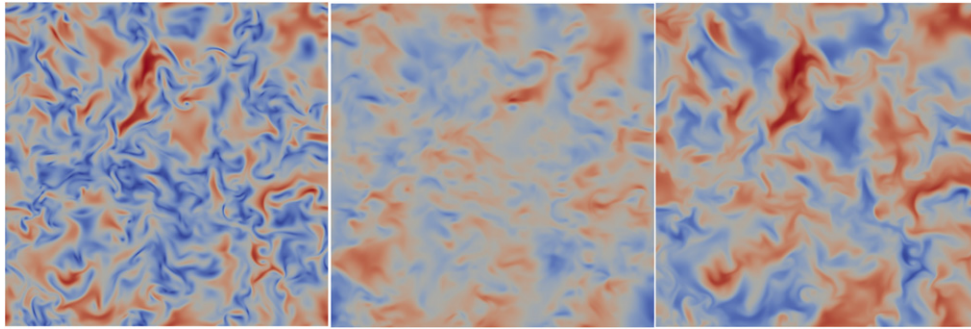
**Figure 12.** Simulation BF: velocity on $z = 0$ plane. From left to right: $|u|$, $u_x$, $u_z$. From blue to red, scales are [0; 0.22] for the velocity norm $|u|$, and [−0.22; 0.22] for the components $u_x$ and $u_z$. Final time of the simulation.
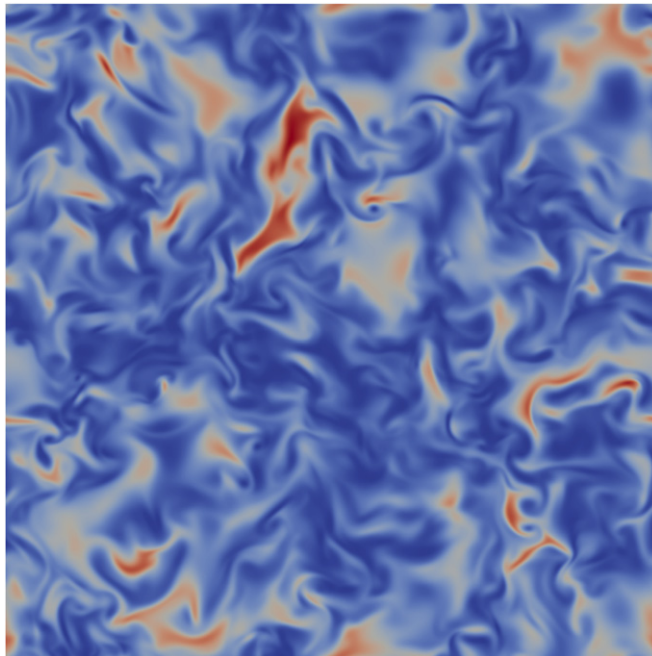


**Figure 13.** Simulation BF: turbulent kinetic energy $k = u_i' u_i'/2$ on the $z = 0$-plane. Final time of the simulation.

## 5.5. Turbulent kinetic energy

Figure 13 displays the turbulent kinetic energy, $k = u_i' u_i'/2$, $0 \leqslant k \leqslant 0.239$, in the $z = 0$-plane, at the final time. The Reynolds fluctuation of the $i$–th velocity component is $u_i'$. Notice the disparity of levels between various regions of the flow; this is an indication of the intermittency.
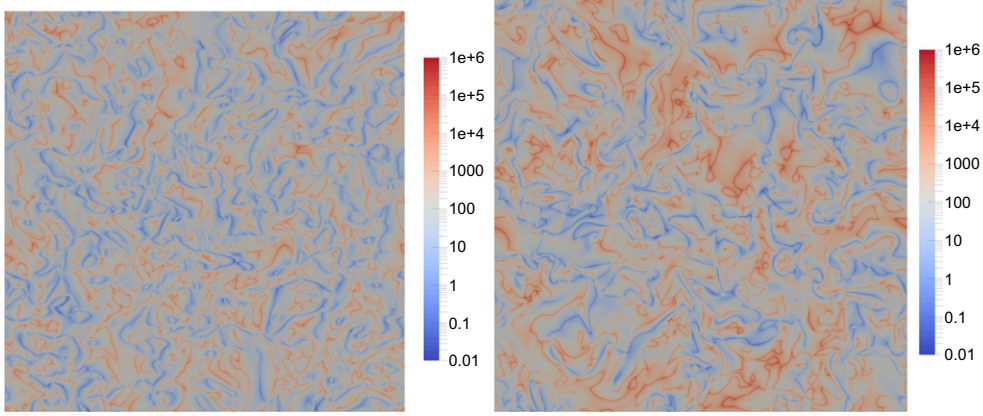
**Figure 14.** Simulation BF: $Re_{\lambda xx}^{3D}=Re \left| \frac{u'_x}{\partial_x u'_x} \right| \sqrt{2k}$ (left) and $Re_{\lambda zz}^{3D}=Re \left| \frac{u'_z}{\partial_z u'_z} \right| \sqrt{2k}$ (right), both on the $z = 0$-plane. Top view and log scales are used. Final time of the simulation.

### 5.6. Taylor-microscale reynolds numbers $Re_\lambda$

The local Taylor-microscale Reynolds numbers, $Re_{\lambda xx}^{3D}$ and $Re_{\lambda zz}^{3D}$, in the horizontal and vertical directions are displayed in figure 14, where the colour scale spans eight orders of magnitude. Let us remark that the same colour scale has been used for these two images although the global vertical Reynolds number is larger than the horizontal one. Consequently, there are more red regions in the right picture than in the left one. Nevertheless the intermittency is clearly revealed by these pictures: the blue corresponds to regions where the fluid is almost at rest, while red corresponds to regions where the Reynolds number is close to $10^6$.

### 5.7. Dissipation rate

The local dissipation rate is defined as $\varepsilon = \nabla_i u_j \, \nabla_i u_j$, and the isosurface of this quantity is given in figure 15 (left). Dissipative structures take the form of sheets, which are denser inside the mixing layer than on the boundaries. On the right-hand side of the same figure, the 2D representation of the dissipation bears a strong resemblance to the vorticity given in figure 9 (left). Figure 16 (left and right) emphasizes the differential dissipation at the altitude $z = 0$ and close to the mixing layer boundary in the heavy fluid. Figure 16 (left) also has to be examined in relationship with figure 14, where the local Reynolds number is displayed.

## 6. Anelastic simulations

Results obtained from two anelastic simulations are now displayed. The first, *AF*, uses At = 0.25 while the second, *AI*, uses a larger Atwood number, At = 0.50, all other parameters being equal.

### 6.1. Simulation AF: At = 0.25

Since the anelastic model contains a rudimentary thermodynamic mode, pressure and temperature are displayed in this section. Two pressure isosurfaces (figure 17) and two temperature isosurfaces (figure 18) are displayed. The pressure isosurfaces do not exhibit a
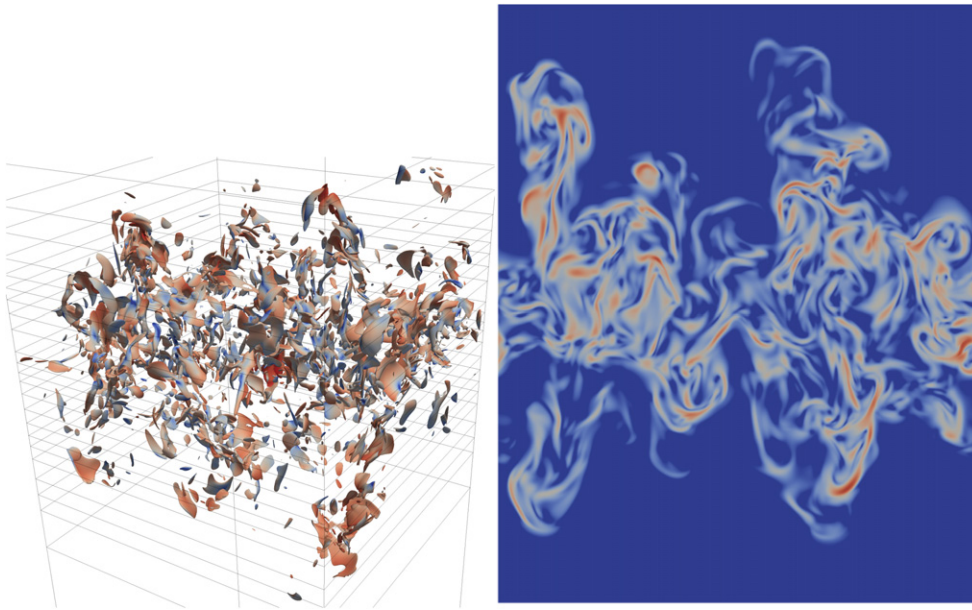
**Figure 15.** Simulation BF. Left: $\varepsilon = 250$ local dissipation rate isosurface coloured by the turbulent kinetic energy (log scale, blue for $k = 5\ 10^{-5}$ and red for $k = 10^{-2}$). Right: dissipation on a $(y, z)$-plane on log scale. Final time of the simulation.
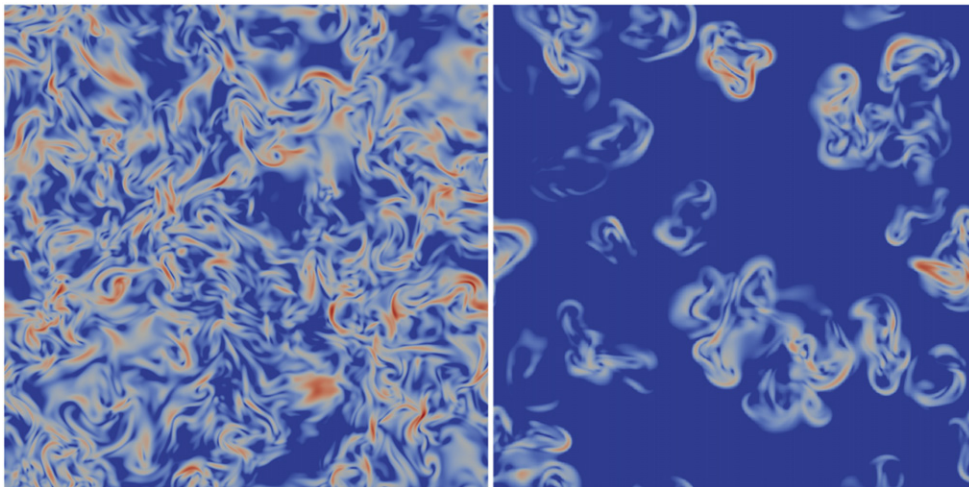


**Figure 16.** Simulation BF: local dissipation rate on the $z = 0$-plane (left) and $z = 0.35$-plane (right). colour log scales are $[10; 1,115]$ (blue to red). Final time of the simulation.

particular pattern although some tori may be distinguished in the top view. Departures from the homothermal initial state ($T^{(initial)}(z) = 1$), of the order of 10%, are induced by the RTI, and the mushroom shape is also recovered for the temperature. Figure 18 left shows a top view of the mixing layer with bubbles cooled, and the image on the right shows a bottom
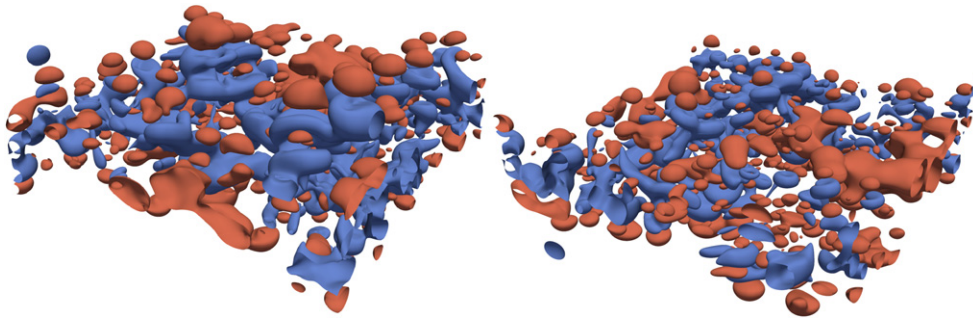
**Figure 17.** Simulation AF: isosurfaces of pressure fluctuation $p' = -0.004$ (blue) and $p' = 0.004$ (red). Left: top view; right: bottom view. Final time of the simulation, where the transition to turbulence has already occurred.
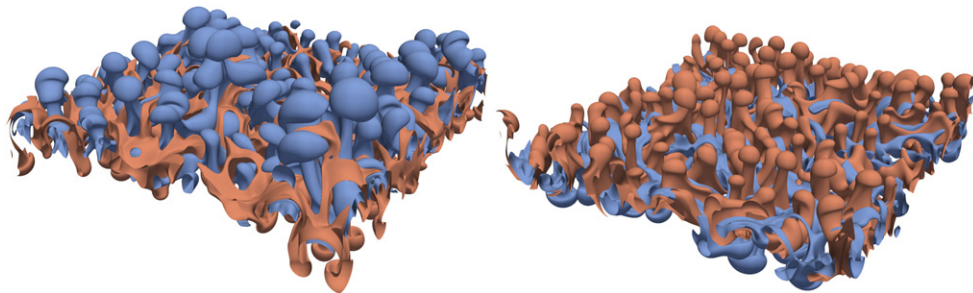


**Figure 18.** Simulation AF: temperature isosurfaces $T = 0.97$ (blue) and $T = 1.03$ (red). Temperature at rest is $T = 1$. Left: top view; right: bottom view. Final time of the simulation.
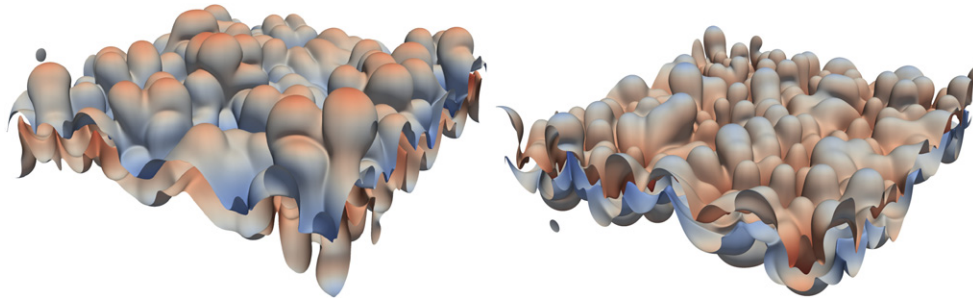


**Figure 19.** Simulation AI: concentration isosurfaces $c = 0.1$ and $c = 0.9$, coloured by the velocity divergence $\partial_i u_i$ (blue: $\partial_i u_i = -0.53$, red: $\partial_i u_i = 0.44$). Final time of the simulation AI, where transition to turbulence is occurring. Left: top view; right: bottom view.

view with spikes slightly heated. The asymmetry between the size of the bubbles and the spikes is also revealed by these two images (Mellado *et al* 2005, George and Glimm 2005, Livescu 2013).
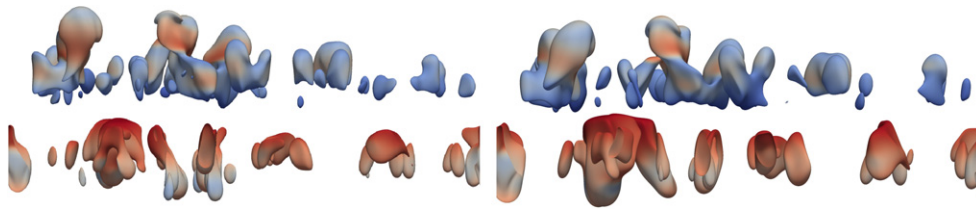
**Figure 20.** Mach number isosurfaces coloured by the concentration. Left: simulation AF (At = 0.25, *Mach* = 0.12), final time of the simulation AF. Right: simulation AI (At = 0.50, *Mach* = 0.15), final time of the simulation AI.
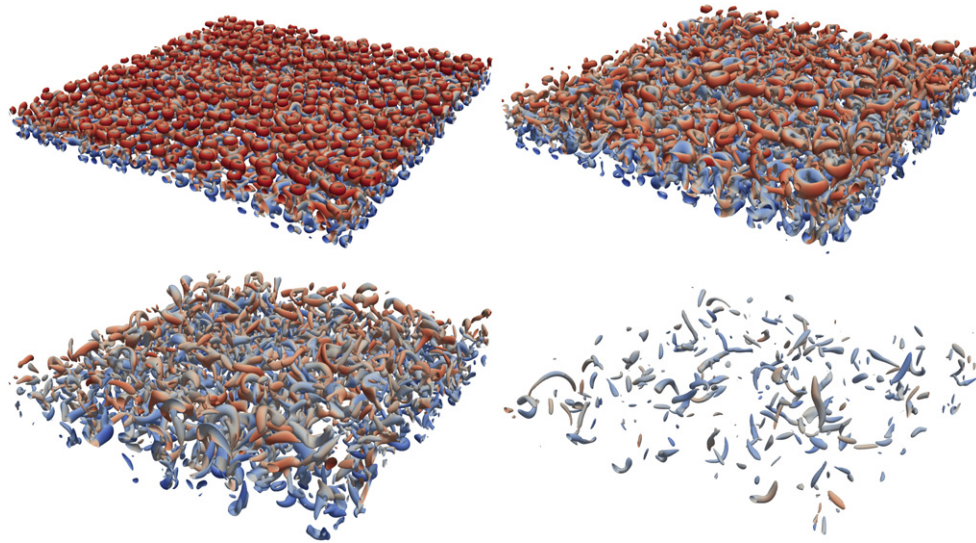


**Figure 21.** Simulation CG: *Q*-criterion isosurfaces ($Q = 5$) coloured by the concentration (heavy fluid in red and light fluid in blue)), at times $t = 1.83$ (top left), 3.05 (top right), 4.45 (bottom left) and 7.74 (bottom right). Vorticity first increases and then decreases in the freely decaying regime. Top view in all four images.

### 6.2. Simulation AI: At = 0.5

For this simulation, only the concentration isosurfaces are displayed in figure 19 at a time where the transition to turbulence is occurring. These surfaces are coloured by the velocity divergence. One then sees on the left large bubbles where the fluid expands and on the right small spikes compressed by the RTI. The larger the Atwood number, the larger the compressibility effects and the larger the asymmetry (George and Glimm 2005, Mellado *et al* 2005).

### 6.3. Mach number effect

The Mach number isosurfaces are displayed in figure 20 for these two anelastic simulations. The strongest Mach number values are located on the boundaries of the mixing layer. On the left, simulation AF is shown at its final time, after the transition to turbulence has occurred. On the right, the simulation AI isosurface appears at its final time, lower than the AF one, and
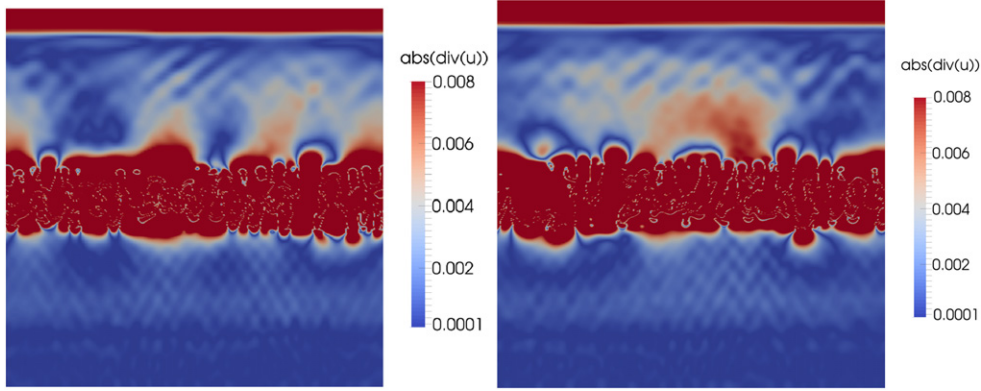
**Figure 22.** Simulation CF: velocity divergence, $|\partial_i u_i|$, on two $(x, z)$-planes at two different $y$-locations. Acoustic wave arrays are visible and at the top, the acoustic wave due to the initialization is also visible.

for a higher value of the Mach number . However, the isosurfaces look similar, which means that compressibility effects grow with the Atwood number.

## 7. Compressible simulations

Two numerical simulations have been carried out with the full NSEs (Gauthier 2013), the characteristics of which are summarized in table 1. The main feature of this configuration is the stratification of the initial equilibrium state. The behavior of the $Sr = 6$ RTI between two stably stratified equilibrium states (see figure 1, right) is the following: first the instability develops and transition to turbulence occurs, then a turbulent mixing layer begins to develop. This is a classical RT regime, which does not seem to be affected by the stratification. Next, the mixing layer starts to smooth the density jump and the effective Atwood number, based on the horizontal mean density profile, decreases. The baroclinic source term and the turbulence production also begin to decrease. During this second regime of stratified RT configurations, the flow reaches a state of freely decaying turbulence in a stabilizing stratification. Density stratification has already been identified as the dominant compressibility effect in mixing layers (Jin *et al* 2005, Mellado *et al* 2005).

### 7.1. Simulation CF: $Re = 3 \times 10^4$

*7.1.1. Q-criterion.* This behavior is illustrated in figure 21 with four images obtained from simulation CF. Isosurfaces of the $Q$-criterion are shown at four different times: $t = 1.83$, where the pure RT regime ends; $t = 3.05$, where the maximum vorticity occurs; $t = 4.45$, where the maximum of the Reynolds number is reached; and $t = 7.74$, where the turbulence is extinguished and the flow vanish. At $t = 1.83$, large-scale vortices are clearly visible while at $t = 3.05$, less structured flow is occurring. At $t = 4.45$ RT patterns are no longer visible and the mixing layer appears as quite homogeneous in the two horizontal directions, while at $t = 7.74$ only a few vortices remain.

*7.1.2. Acoustics.* These two simulations carried out with the full NSEs exhibit strong acoustic production, essentially in the heavy fluid, which is revealed by slices of the velocity
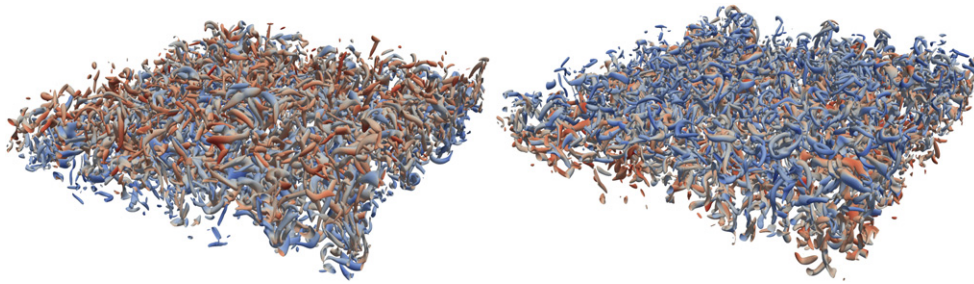
**Figure 23.** Simulation CG: $Q$-criterion isosurfaces with $Q = 10$ coloured by the concentration (heavy fluid in red and light fluid in blue). Left: top view, right: bottom view. Time at which the vorticity is at a maximum.

divergence as shown in figure 22. In both the heavy and light fluids, acoustic wave arrays are visible.

### 7.2. Simulation CG: $Re = 6 \times 10^4$

This series of RT flow visualizations ends with the $Q$-criterion isosurfaces of the compressible simulation CG. Only two isosurfaces are shown in figure 23, at the time where the maximum vorticity occurs. Like the previous simulation, it shows an intricate set of vortices stirring the heavy and light fluids. It is worth noticing that mixing layers generated between two stably stratified equilibrium states are strongly homogeneous. Indeed if a blob of fluid escapes upward the mixing layer, it is surrounded by lighter fluid, and by heavier fluid if the blob moves downward. In both cases, acceleration acts as a restoring force.

## 8. Conclusion

We have visualized some Rayleigh–Taylor mixing flows between miscible fluids computed with Boussinesq and anelastic models and with the full Navier–Stokes equations. This visualization helps in understanding the structure—such as the vortical structure—of Rayleigh–Taylor flows. These visualizations also lead to some conclusions and remarks, which may be summarized as follows:

(i) For a single-mode Rayleigh–Taylor instability, the vorticity norm leads to a toroidal isosurface, while the horizontal components lead to a 'double-spoon' pattern. However vortices are better detected by the $Q$-criterion, which has been used systematically in this work.

(ii) Large vortical structures, with the torus corresponding to a mushroom pattern, appear clearly on the boundaries. However, inside the mixing layer, the Rayleigh–Taylor patterns disappear, and the vortical structures tend to be oblong or take the form of short filaments.

(iii) Turbulent kinetic energy and local Taylor-microscale Reynolds number clearly show the intermittent character of the flow. In some regions the fluid is almost at rest, while in others the Reynolds number is close to $10^6$. As a result, there are some unmixed regions.

(iv) Dissipative structures take the form of sheets, which are denser inside the mixing layer than on the boundaries.

(v) Anelastic simulations reveal the asymmetry between the sizes of bubbles and spikes at an Atwood number equal to 0.25 and more clearly for Atwood number 0.50. They also show

the cooled expanded bubbles versus the heated compressed spikes. Moreover, the strongest Mach number values are located on the boundaries of the mixing layer.

*(vi)* Simulations carried out with the full Navier–Stokes equations show a two-step phenomenon: first turbulence and vorticity increase, which smooths out the density jump. In the second step, turbulence is in a freely decaying regime.

*(vii)* Mixing layers generated between two stably stratified equilibrium states are strongly homogeneous in the horizontal directions. A strong acoustic production is also observed.

Finally, let us suggest that the Rayleigh–Taylor instability deserves to be studied from the point of view and with the tools of topological fluid dynamics (Bajer *et al* 2013).

## Acknowledgments

## References

http://en.wikipedia.org/wiki/scientific_visualization

Etiene T, Nguyen H, Kirby R M and Silva C T 2013 "Flow visualization" juxtaposed with "Visualization of flow" Synergistic opportunities between two communities 51st AIAA Aerospace Sciences Meeting, (7–10 January 2013, Grapevine, TX) *AIAA J.* **2013-1163** 1–3

Hertzberg J and Sweetman A 2005 Images of fluid flow: Art and physics by students *J. Visualization* **8** 145–52

http://iwpctm.org/

Borland D and Taylor R M II 2007 Rainbow color map still considered harmful *IEEE Comput. Graph. Appl.* **27** 14–7

Moreland K 2009 Diverging color maps for scientific visualization expanded *Advances in Visual Computing* **5876** 92–103

Jeong J and Hussain F 1995 On the identification of a vortex *J. Fluid Mech.* **285** 69–95

Dubief Y and Delcayre F 2000 On coherent-vortex identification in turbulence *J. Turb.* **11** 1–22

Schneider N, Hammouch Z, Labrosse G and Gauthier S 2015 A spectral anelastic Navier–Stokes solver for a stratified two-miscible-layer system in infinite horizontal channel *J. Comput. Phys.* **299** 374–403

Glimm J, Li X L, Menikoff R, Sharp D H and Zhang Q 1990 A numerical study of bubble interactions in Rayleigh–Taylor instability for compressible fluids *Phys. Fluids* A **2** 2046–54

Mellado J P, Sarkar S and Zhou Y 2005 Large-eddy simulation of Rayleigh–Taylor turbulence with compressible miscible fluids *Phys. Fluids* **17** 076101–20

George E and Glimm J 2005 Self-similarity of Rayleigh–Taylor mixing rates *Phys. Fluids* **17** 054101–13

Jin H, Liu X F, Lu T, Cheng B, Glimm J and Sharp D H 2005 Rayleigh–Taylor mixing rates for compressible flow *Phys. Fluids* A **17** 024104–10

Livescu D 2013 Numerical simulations of two-fluid turbulent mixing at large density ratios and applications to the Rayleigh–Taylor instability *Phil. Trans. R. Soc.* A **371** 20120185–23

Chu B-T and Kovásznay L S G 1957 Non-linear interactions in a viscous heat-conducting compressible gas *J. Fluid Mech.* **3** 494–514

http://paraview.org/

Abarzhi S I, Gauthier S and Sreenivasan K R 2013 Turbulent mixing and beyond: non-equilibrium processes from atomistic to astrophysical scales II, introduction *Phil. Trans. R. Soc.* A **371** 20130268–7

http://tmbw.org/

Schneider N and Gauthier S 2015 Asymptotic analysis of Rayleigh–Taylor flow for Newtonian miscible fluids *J. Eng. Math.* **92** 55–71

Gauthier S, Le Creurer B, Abéguilé F, Boudesocque-Dubois C and Clarisse J-M 2005 A self-adaptive domain decomposition method with Chebyshev method *Int. J. Pure Appl. Math.* **24** 553–77

Le Creurer B and Gauthier S 2008 A return toward equilibrium in a two-dimensional Rayleigh–Taylor flows instability for compressible miscible fluids *Theor. Comput. Fluid Dyn.* **22** 125–44

Mueschke N J, Andrews M J and Schilling O 2006 Experimental characterization of initial conditions and spatio-temporal evolution of a small-Atwood-number Rayleigh–Taylor mixing layer *J. Fluid Mech.* **567** 27–63

Mueschke N J and Schilling O 2009 Investigation of Rayleigh–Taylor turbulence and mixing using direct numerical simulation with experimentally measured initial conditions: I. Comparison to experimental data *Phys. Fluids* **21** 014106–19

Glimm J, Sharp D H, Kaman T and Lim H 2013 New directions for Rayleigh–Taylor mixing *Phil. Trans. R. Soc.* A **371** 20120183–17

Waddell J T, Niederhaus C E and Jacobs J W 2001 Experimental study of rayleightaylor instability: Low atwood number liquid systems with single-mode initial perturbations *Phys. Fluids* **13** 1263–73

Schneider N 2015 Vorticité et mélange dans les écoulements de Rayleigh–Taylor turbulents, en approximation anélastique et de Boussinesq *PhD Thesis* Université de Paris VI

Schneider N and Gauthier S 2015 Vorticity and mixing in Rayleigh–Taylor Boussinesq turbulence *Submitted*

Young Y N, Tufo H, Dubey A and Rosner R 2001 On the miscible Rayleigh–Taylor instability two and three dimensions *J. Fluid Mech.* **447** 377–408

Ristorcelli J R and Clark T T 2004 Rayleigh–Taylor turbulence: self-similar analysis and direct numerical simulations *J. Fluid Mech.* **507** 213–53

Vladimirova N and Chertkov M 2009 Self-similarity and universality Rayleigh–Taylor, Boussinesq turbulence *Phys. Fluids* **21** 015102–9

She Z-S, Jackson E and Orszag S A 1990 Intermittent vortex structures in homogeneous isotropic turbulence *Nature* **344** 226–8

Gauthier S 2013 Compressibility effects in Rayleigh–Taylor flows: influence of the stratification *Phys. Scr.* **T155** 014012–8

Bajer K, Kimura Y and Moffatt H K 2013 Topological fluid dynamics: theory and applications *Procedia IUTAM* **7** 1–2